Catal Lett (2009) 127:107–112
DOI 10.1007/s10562-008-9649-4

NO_x Storage at Low Temperature over MnO_x–SnO_2 Binary Metal Oxide Prepared Through Different Hydrothermal Process

Lisi Wei · Junhua Li · Xingfu Tang

Received: 15 July 2008 / Accepted: 8 September 2008 / Published online: 11 October 2008

Abstract Three MnO_x–SnO_2 catalysts were successfully prepared by hetero-redox, homo-redox and common hydrothermal methods. NO adsorption and desorption were performed to investigate the NO_x storage capacity at 100 °C. All the samples showed good performances on NO_x storage, especially the sample prepared by homo-redox hydrothermal method. The XRD, BET, TPR, XPS measurements were used to characterize the structure of the catalysts. The results revealed that the oxidation state of Mn and the defect oxygen species could be responsible for the high NO_x storage capacity.

Keywords Hydrothermal method · MnO_x–SnO_2 · NSR · NO_x storage capacity

1 Introduction

NO_x storage and reduction (NSR) technique was originally developed by TOYOTA Company and considered to be the most promising way to remove NO_x under lean-burn conditions [1–3]. A typical NSR catalyst consisted of three parts: precious metal as an oxidative and reductive, alkali or alkaline-earth oxide as a storage component and support, for example $Pt/BaO/Al_2O_3$ [4–6]. Under lean-burn condition, NO was oxidized to NO_2 and stored in the catalyst. When the engine was switched to rich-burn conditions, NO_x was released and reduced to N_2 by reductive gas in the exhaust. However, NO was very stable and difficult to oxidize at low temperature. Therefore, transition metal oxides with strong oxidation ability and low expense have attracted much attention, especially manganese oxides. NO adsorption on MnO_x–CeO_2 at low temperature was studied by Mashida [7]. The results showed that MnO_x–CeO_2 had formed a fluorite-type solid solution and the NO_x trapping capacity was related to the adjacent pair sites (Mn and Ce). Ce ions provided a number of adsorption sites on the surface. Manganese ions substituted in the CeO_2 lattice acted as not only a catalyst for NO oxidation in the presence of O_2, but also an oxidation agent for NO when O_2 partial pressure became low. Canevali et al. [8] studied the mechanism on NO interaction with SnO_2 by paramagnetic resonance and Mössbauer spectroscopy technology. The results revealed that the NO interaction with SnO_2 involved electron injection to SnO_2, formation of oxygen vacancies, and chemisorptions of NO_2^- and NO_3^- anions. It demonstrated that SnO_2 shows the strong interaction with NO, which might be favored for Mn reacting with NO. However, a MnO_x–SnO_2 binary metal oxide for NO_x storage has not been reported in the past decades.

Different preparation methods caused different crystal structure, specific surface areas, redox ability and catalytic activity. In this work, MnO_x–SnO_2 binary metal oxides were prepared by three hydrothermal methods. The XRD, BET, TPR, XPS, NO-adsorption and TPD measurements were used to characterize the structure and NO_x storage capacity of the catalysts.

2 Experimental

2.1 Preparation

MnO_x–SnO_2 catalysts with a certain molar ratio of $Mn/(Mn + Sn) = 0.4$ were synthesized by three hydrothermal method:

L. Wei · J. Li (✉) · X. Tang
Department of Environmental Science and Engineering, Tsinghua University, Beijing 100084, China
e-mail: lijunhua@tsinghua.edu.cn

(i) Hetero-redox hydrothermal,

$$HSnO_2^- + 3OH^- + H_2O - 2e \rightarrow Sn(OH)_6^{2-} \quad E^\theta = 0.93\,V \tag{1}$$

$$MnO_4^- + 2H_2O + 3e \rightarrow MnO_2 \downarrow + 4OH^- \quad E^\theta = 0.60\,V \tag{2}$$

$$2KMnO_4 + 3SnCl_2 + 4KOH + 4H_2O = 3Sn(OH)_4 \downarrow + 2MnO_2 \downarrow + 6KCl \tag{3}$$

(ii) Homo-redox hydrothermal,

$$2KMnO_4 + 3MnCl_2 + 4KOH = 5MnO_2 \downarrow + 6KCl + 2H_2O \tag{4}$$

$$SnCl_4 + 4KOH = Sn(OH)_4 \downarrow + 4KCl \tag{5}$$

(iii) Common hydrothermal,

$$SnCl_4 + 4KOH = Sn(OH)_4 \downarrow + 4KCl \tag{6}$$

$$2MnCl_2 + 4KOH + O2 = 2MnO(OH)_2 \downarrow + 4KCl \tag{7}$$

and the catalysts were donated as HH, MH and CH, respectively.

In the preparation, the certain amount of chemical reagents as list in Table 1 and 70 mL deioned water were put into the Teflon-lined stainless autoclaves with 100 mL capacity, and then the autoclaves were sealed and kept at 160 °C for 24 h. They were allowed to cool to room temperature naturally. The precipitation were filtered and washed by deioned water for several times until Cl^- cannot be found (tested by $AgNO_3$ solution). The cakes were dried at 110 °C for 12 h and then calcined at 500 °C for 5 h in the air. The yields of final product were above 90% (calculated on the assumption of MnO_2-SnO_2). Finally, the samples were crushed and sieved to 40–60 mesh for NO_x storage experiments.

2.2 Characterization

The X-ray diffraction (XRD) patterns of the catalysts were obtained with a Bruker D8 Advance X-ray diffractometer using Cu Kα ($\lambda = 1.5418$ Å) radiation and operated at 40 kV and 40 mA.

BET surface areas were measured by N_2 adsorption at 77.3 K using a Quantachrome QuadraSorb SI instrument. Prior to the analysis, the samples were degassed at 573 K for 2 h. The specific surface area was determined from the linear part of the BET equation.

Temperature-programmed Reduction (TPR) experiments were conduced on a Micromeritics ChemiSorb 2720 using approximately 20 mg of samples. After pretreated at 300 °C in N_2 for 1 h, the samples were cooled down to room temperature. The reducing gas, a mixture of 10% H_2/Ar, at a flow rate of 50 mL/min, was used to reduce the catalysts from room temperature to 900 °C with a temperature ramp of 10 °C/min. The consumed H_2 was calculated by integration of the corresponding TCD signal intensities.

X-ray photoelectron spectroscopy (XPS) data were obtained with an ESCALab220i-XL electron spectrometer from VG Scientific using 300 W Mg Kα radiation. The base pressure was about 3×10^{-9} mbar. The binding energies were referenced to the C 1s line at 284.8 eV from adventitious carbon. Binding energies (BE) were measured for C 1s, O 1s, Mn 2p, Mn 3s, and Sn 3d. The spectra were calculated using the XPSPEAK program by the curve fitting with a Gaussian/Lorentzian ratio of 90/10 after smoothing and subtraction of the Shirley-type background.

2.3 NO Adsorption/Desorption

NO adsorption experiments were carried out in a U-type quartz reactor with inner diameter of 5 mm under normal atmospheric pressure employing 0.5 g catalyst. The samples were pretreatment in 8% O_2/N_2 at a total flow rate 400 mL/min at 500 °C for 30 min, and then cooled to 100 °C in N_2 for adsorption. When the temperature stabilized at 100 °C, a mixture gas including 500 ppm of NO, 8% O_2 and balanced N_2 at 400 mL/min passed through the samples for 45 min. During this time, the NO–NO_2–NO_x concentration in the outlet stream was recorded by an online Chemiluminescence NO–NO_2–NO_x analyzer (42C High Level, Thermo Electron Corporation).

After adsorption for 45 min, NO and O_2 were cut, and pure nitrogen (400 mL/min) was introduced for 1 h to remove the weakly adsorbed species at the catalysts' surface. And then Temperature-programmed Desorption

Table 1 Preparation condition of MnO_x–SnO_2 catalysts

Method	$KMnO_4$ (mmol)	$MnCl_2$ (mmol)	$SnCl_2 \cdot 2H_2O$ (mmol)	$SnCl_4 \cdot 5H_2O$ (mmol)	KOH (mmol)	KCl[a] (mmol)
HH	5.0	–	7.5	–	10.0	25.0
MH	2.0	3.0	7.5	–	34.0	4.0
CH	–	5.0	–	7.5	40.0	–

[a] KCl was added to autoclave to keep the same concentration of K^+ and Cl^-

(TPD) experiments were performed by ramping the temperature from room temperature to 500 °C at 10 °C/min with 400 mL/min N_2. The concentration of NO, NO_2, and NO_x in the outlet stream were also collected by NO–NO_2–NO_x analyzer. The NO_x storage capacity (NSC) was calculated according to the integral area of desorption profile.

3 Results and Discussion

3.1 Characterization of MnO_x–SnO_2 Catalysts

Figure 1 showed the XRD patterns of the samples. All samples appeared the typical peaks of tetragonal rutile-type SnO_2 (JCPDS #71-0652). Especially the MnO_x–SnO_2 catalyst prepared by common hydrothermal methods (CH), no distinct diffraction of manganese oxides was observed. In previous literature [9], it was thought that two reasons might be responsible for this phenomenon. One was manganese oxide highly dispersed on the surface of SnO_2, the other was Mn ions entered the SnO_2 lattice to form solid solution. However, in the present work, the CH catalyst was synthesized with a certain molar ratio of Mn/(Mn + Sn) = 0.4 which much higher than the general monolayer dispersion capacity [10]. Therefore, there was a possibility that the different components in the samples admixed into each other in bulk. No Mn oxides detected by XRD was not mainly due to the formation of monolayer on the surface of SnO_2, but could be due to the following reason, the doping of Mn ions into the crystal lattice of rutile SnO_2 [9]. Surface atomic ratios of samples were illustrated in Table 2. From Table 2, it can be seen that the surface atomic ratio of CH sample (0.25) was smaller than theoretical value (0.4). It supported our assumption of formation of MnO_x–SnO_2 solid solution from another aspect.

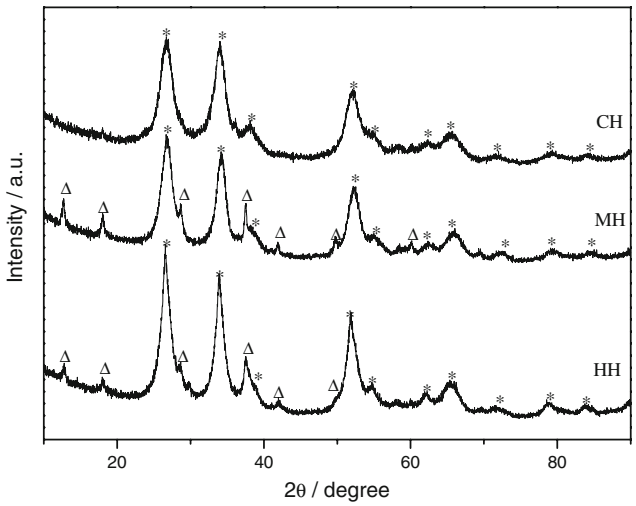

Fig. 1 XRD patterns of MnO_x–SnO_2 catalysts prepared by various methods ((*) SnO_2, (△) MnO_2)

Sample MH and HH showed both similar diffraction patterns. Peaks at $2\theta = 12.7, 18.1, 28.7, 42°$ corresponded to the main diffraction peaks of α-MnO_2 (JCPDS #44-0141). Compare with MH sample, sharper and higher intensity peaks of SnO_2 were detected in HH sample, indicating it crystallized better. These great differences were caused by the various preparation methods. From the equation of (1) and (2), it can be easily seen that input KOH could accelerate the reaction 1 and inhibit the reaction 2. Consequently, $SnCl_2$ would hydrolyze firstly and generate white precipitation under the alkali condition, and then electron transferred from $HSnO_2^-$ to MnO_4^-. Finally, the sample formed a core-like structure. On one hand, SnO_2 crystal inner core grow larger and better. This was in good agreement with XRD results. On the other hand, Mn precipitate partly covered on the surface of Sn precipitate. XPS results about surface atomic ratio of sample HH showed that the ratio value of Mn/(Mn + Sn) was bigger than others. It provided additional proof to testify our explanation of reaction process.

The BET surface areas of the samples were listed in Table 2. The results of BET measurements suggested that the surface areas of MnO_x–SnO_2 catalysts were related to preparation methods, and the HH catalyst showed the minimum surface area. Its low surface area was in good agreement with its large particle size and high crystallinity as discussed above.

TPR experiments were carried out to investigate the reducibility of the MnO_x–SnO_2 catalysts (Fig. 2) and to determine the oxidation state of Mn from the peak area, which was calibrated with the reduction of AgO (Table 2). According to calculated results, it can be concluded that Mn^{4+} was the main Mn species in the HH and MH

Table 2 BET surface areas, TPR results and NO_x storage properties of MnO_x–SnO_2 catalysts

Sample	$S_{(BET)}$ (m^2/g)	Mn/(Mn + Sn)[a]	Consumed H_2 (mmol/g)	Oxidation state of Mn	NO_x storage capacity (μmol/g)
HH	67.0	0.45	13.8	4.2	236
MH	83.1	0.35	13.4	4.1	290
CH	83.2	0.25	11.7	3.1	194

[a] The surface atomic ratios of samples were obtained from XPS measurements

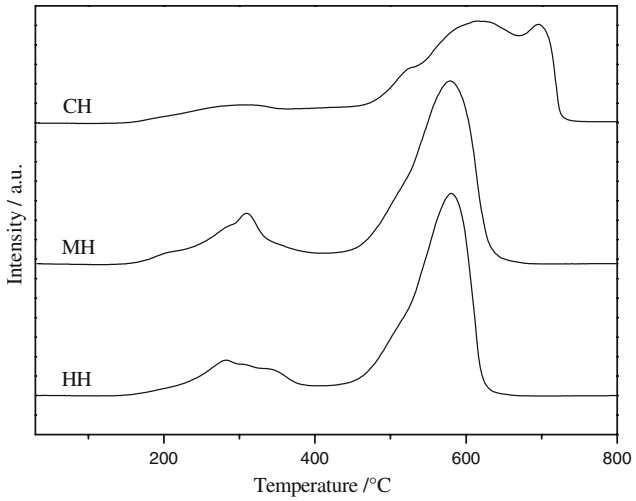

Fig. 2 H_2-TPR profiles of MnO_x–SnO_2 catalysts prepared by various methods

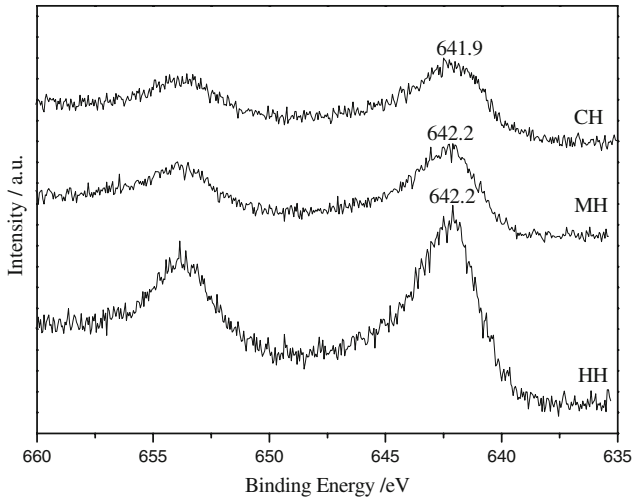

Fig. 3 Mn 2p XPS spectra of MnO_x–SnO_2 catalysts prepared by various methods

catalysts while Mn^{3+} could be the dominant Mn species in the CH catalyst.

According to reference [11], pure SnO_2 showed one overlapped reduction peak at 700–760 °C which can be ascribed to the reduction of SnO_2 into metallic Sn. In general, the reduction of MnO_2 and Mn_2O_3 were followed a typical two-step process ($MnO_2 \rightarrow Mn_3O_4 \rightarrow MnO$, $Mn_2O_3 \rightarrow Mn_3O_4 \rightarrow MnO$) [12]. Therefore, the reduction peak below 400 °C should be assigned to the reduction of MnO_2 or Mn_2O_3 to Mn_3O_4 and the overlapped peak in the temperature range of 450–750 °C could be attributed to the reduction of Mn_3O_4 to MnO, SnO_2 to SnO and SnO to Sn. Compared the position of peaks, it can be easily obtained that the HH and MH catalysts with main Mn species of Mn^{4+} were liable to be reduced and might be beneficial to NO oxidizing.

The XPS spectra of Mn 2p, Mn 3s, O 1s and Sn 3d were measured for these three samples and the results were summarized in Table 3. The binding energy of Sn $3d_{5/2}$ peaks centered around 486.5 eV for all samples were characteristic of Sn^{4+}, which was in good agreement with XRD data.

From the spectra of Mn 2p (Fig. 3), for HH and MH catalyst, the BE peak at 642.2 eV (Mn $2p_{3/2}$) could be ascribed to Mn^{4+}. The binding energy of Mn $2p_{3/2}$ peak centered at 641.9 eV for sample CH probably corresponded to the Mn^{3+} state. However, the variation of XPS binding energies of Mn 2p alone, from Mn^{2+} to Mn^{4+}, was too narrow (less than 1.0 eV) to precisely evaluate the Mn valence [13]. Therefore, the extent of Mn 3s multiplet splitting measured simultaneously (Mn 3s ΔE) offered additional insights into the Mn chemical states. The results summarized in Table 3 were consistent with XRD and H_2-TPR measurements.

The XPS spectra of O 1s were shown in Fig. 4. Two peaks (O_α and O_β) could be clearly observed in the O 1s spectra, which represented two different kinds of surface oxygen species. The binding energy of 529–530 eV was the characteristic of the lattice oxygen (O^{2-}) [14] and the binding energy of 531–533 eV might be assigned to the defect oxide or the surface oxygen ions with low coordination [15]. The different preparation methods result in remarkable differences of oxidation state of Mn and the concentration of O_β. In the HH and MH catalysts, manganese species were dominantly presented as Mn^{4+}, whereas Mn^{3+} was the dominant species in the CH catalyst. And the corresponding concentrations of O_β were 59.3, 75.7 and 31.2%, respectively. It revealed that hetero-redox and homo-redox hydrothermal methods could apparently increase the concentration of the defect oxides

Table 3 XPS results of MnO_x–SnO_2 catalysts

Sample	BE (eV)			Mn 3s ΔE (eV)	Oxidation state of Mn	O 1s		$O_\beta/(O_\alpha + O_\beta)$ (%)
	Mn $2p_{3/2}$	Mn 3s	Sn $3d_{5/2}$			O_α	O_β	
HH	642.2	84.1	486.5	4.5	4.0	530.0	531.3	59.3
MH	642.2	84.0	486.4	4.5	4.0	529.8	531.0	75.7
CH	641.9	83.8	486.7	5.3	3.0	530.4	532.2	31.2

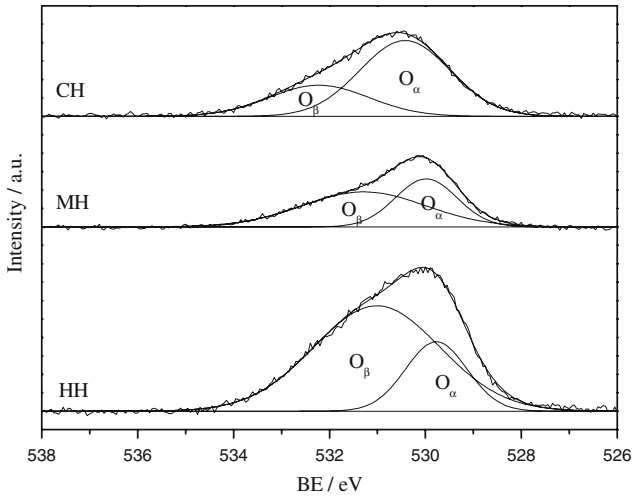

Fig. 4 O 1s XPS spectra of MnO_x–SnO_2 catalysts prepared by various methods

on the surface in contrast to common hydrothermal method, especially homo-redox hydrothermal method. Therefore, the MH sample possessed the richest defect oxygen species.

3.2 NO Adsorption/Desorption Performance of MnO_x–SnO_2 Catalysts

The curves of NO adsorption at 100 °C on samples were presented in Fig. 5. NO_x was not detected in the effluent in the initial 9–10 min for the HH and MH sample while only 5 min for the CH catalyst. After breakthrough, NO_x concentration in the outlet stream was gradually recovered to approximate 500 ppm, including 340–370 ppm NO and 130–160 ppm NO_2. Compared to reference [16], NO_2 in

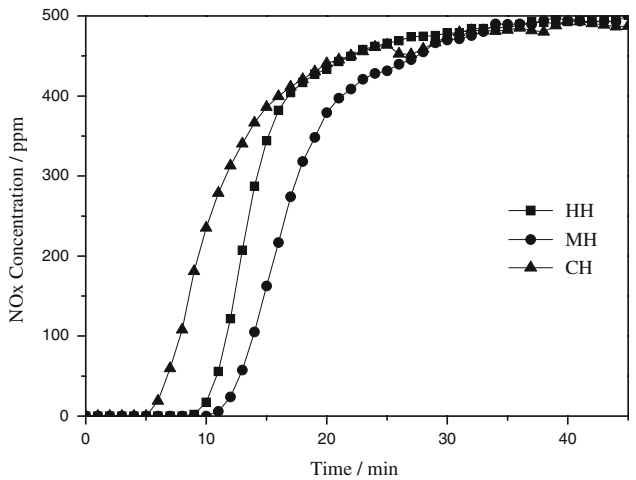

Fig. 5 NO_x adsorption curves on MnO_x–SnO_2 catalysts prepared by various methods at 100 °C (NO = 500 ppm, O_2 = 8 vol.%, N_2 as balance, F/W = 48,000 $cm^3\ h^{-1}\ g^{-1}$)

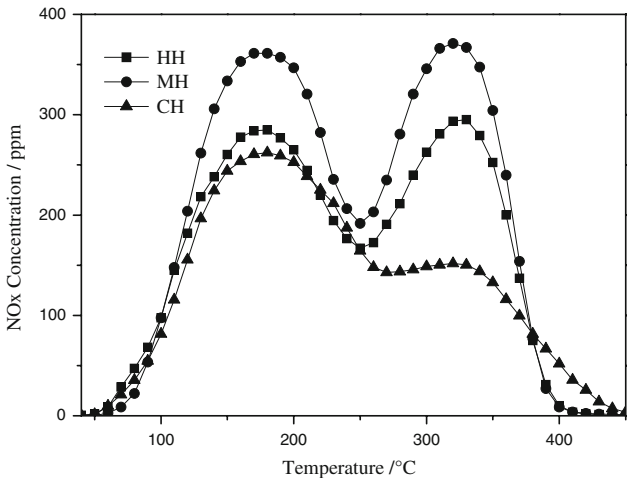

Fig. 6 NO_x desorption curves of MnO_x–SnO_2 catalysts prepared by various methods

the downstream was found at a higher concentration, demonstrating higher conversion of NO to NO_2 at 100 °C in the presence of O_2. It suggested that the catalysts prepared in this work had strong oxidation ability which was beneficial to adsorption NO_x at low temperature. Combined with the data of NO_x storage capacity in Table 2, it can be concluded that the NSC of samples followed the decreased order: MH > HH > CH. This phenomenon was agreement with the possession of O_β of the samples, indicating the defect oxygen species might play an important role in the NO_x adsorption. Mashida M. found that the increased low-temperature desorption was associated with the oxygen vacancy which produced by lattice substitution [7].

Figure 6 displayed the NO_x desorption curves of different samples previously adsorbed NO at 100 °C for 45 min. NO_x desorption followed a two-step process, one desorption peak was at the low-temperature around 160 °C and the other was at the higher-temperature around 320 °C, which was similar with the reference [16]. However, the HH and MH sample showed a bigger NSC than the CH sample on the higher-temperature peak, which can be interpreted by the oxidation state of Mn. Higher oxidation state of Mn had higher oxidation ability, thus more stable nitrate species formed on the surface as a result of more NO_x desorpted at the higher temperature. Compared with MH catalyst, HH catalyst showed the similar peak shape and position but only lower peak height, which may be due to the defect oxygen species on the surface of samples.

4 Conclusions

Three MnO_x–SnO_2 catalysts for NO_x storage at 100 °C were successfully prepared by different hydrothermal processes. The NSC of the samples followed the decreased

order: MH > HH > CH. The characterized results revealed that the higher oxidation state of Mn should be the main reason for the higher NO_x storage capacity of catalyst HH and MH. Compared to the HH catalyst, the MH catalyst displayed better performance on NO_x storage, which might be correspond to the concentration of the defect oxygen species.

Acknowledgments The research was financially supported by the National Natural Science foundation of China (Grant NO. 20507012), the National High-Tech Research and Development (863) Program of China (Grant No. 2006AA060301) and New Century Excellent Talents in University of China (NCET-2005).

References

1. Takahashi N, Shinjoh H, Iijima T, Suzuki T, Yamazaki K, Yokota K, Suzuki H, Miyoshi N, Matsumoto S, Tanizawa T, Tanaka T, Tateishi S, Kasahara K (1996) Catal Today 27:63
2. Kašpar J, Fornasiero P, Hickey N (2003) Catal Today 77:419
3. Katoh K, Kihara T, Asanuma T, Gotoh M, Shibaki N (1995) Toyota Technol Rev 44:27
4. Shinjoh H, Takahashi N, Yokota K, Sugiura M (1998) Appl Catal B 15:189
5. Su Y, Amiridis MD (2004) Catal Today 96:31
6. Zhou G, Luo T, Gorte RJ (2006) Appl Catal B 64:88
7. Machida M (2002) Catal Surv Jpn 5:91
8. Canevali C, Mari CM, Mattoni M, Morazzoni F, Ruffo R, Scotti R, Russo U, Nodari L (2004) Sens Actuators B 100:228
9. Wang X, Xie YC (2001) Catal Lett 75:73
10. Xie YC, Tang YQ (1990) Adv Catal 37:1
11. Wang X, Xie YC (2001) React Kinet Catal Lett 72:229
12. Shi LM, Chu W, Qu FF, Luo SZ (2007) Catal Lett 113:59
13. Ramesh K, Chen LW, Chen FX, Liu Y, Wang Z, Han YF (2008) Catal Today 131:477
14. Hamoudi S, Larachi F, Adnot A, Sayari A (1999) J Catal 185:333
15. Larachi F, Pierre J, Adnot A, Bernis A (2002) Appl Surf Sci 195:236
16. Yu JJ, Tao YX, Liu CC, Hao ZP, Xu ZP (2007) Environ Sci Technol 41:1399